Transition from viscous fingers to foam during drainage in heterogeneous porous media ⓔⓟ ✓

Federico Lanza ✉ ⓘ ; Santanu Sinha ⓘ ; Alex Hansen ⓘ ; Alberto Rosso ⓘ ; Laurent Talon ⓘ

Check for updates

CrossMark

View Online

Export Citation

Physics of Fluids

Special Topic:
Flow and Civil Structures

Submit Today

AIP Publishing

Transition from viscous fingers to foam during drainage in heterogeneous porous media (EP)

View Online   Export Citation   CrossMark

Federico Lanza,[1,2,a] (iD) Santanu Sinha,[3] (iD) Alex Hansen,[2] (iD) Alberto Rosso,[1] (iD) and Laurent Talon[1] (iD)

AFFILIATIONS

[1]Université Paris-Saclay, CNRS, LPTMS, 91405 Orsay, France
[2]PoreLab, Department of Physics, Norwegian University of Science and Technology, N-7491 Trondheim, Norway
[3]PoreLab, Department of Physics, University of Oslo, N-0316 Oslo, Norway

[a]Author to whom correspondence should be addressed: federico.lanza.5@gmail.com

ABSTRACT

We investigate the behavior of drainage displacements in heterogeneous porous media finding a transition from viscous fingering to foam-like region. A pore network model incorporating the formation of blobs is adopted to study this phenomenon. By imposing a pressure difference between the inlet and outlet, we observe that the displacement pattern undergoes a significant transition from a continuous front of growing viscous fingers to the emergence of foam, which develops and propagates until breakthrough. This transition occurs at a specific distance from the inlet, which we measure and analyze as a function of the viscosity ratio and the capillary number, demonstrating that it follows a non-trivial power-law decay with both the parameters. Moreover, we discuss the relationship between the evolution of the total flow rate and the local pressure drop, showing that the foam developed reduces global mobility. We observe that foam is formed from the fragmentation of viscous fingers beneath the front, and this instability mechanism is connected with fluctuations of the local flow rate, which we analyze both in the viscous fingering region and in the foam region.

I. INTRODUCTION

Simultaneous flow of multiple immiscible fluids in porous media, named multi-phase flow,[1–3] is involved in a wide range of industrial and geophysical applications. A few important examples, for instance, are the understanding of the water cycle, the transport of pollutants in soils, oil recovery, geothermal energy extraction, and carbon dioxide sequestration. In a two-phase flow, when a more wetting fluid displaces a less wetting fluid inside a porous medium, the flow is referred to as imbibition, whereas the opposite case, when a less wetting fluid displaces a more wetting fluid, it is called drainage.[4] The study we present here deals with drainage, and we will refer the more- and less-wetting fluids as wetting and non-wetting fluids, respectively. Depending on flow parameters and system properties, the displacement process produces fronts with distinct shapes, which characterize the underlying flow mechanism.[5] There can be stable displacement with flat front[6] when a fluid of high viscosity invades a fluid with much lower viscosity under a viscous pressure drop, or, there can be more complex fingering patterns displaying fractal structures.[3,7] Two essential mechanisms control the shape of the fingers. First, there is viscous fingering,[8–10] which is an instability that occurs during the fast displacement of a low-viscosity fluid injected into a more viscous fluid.[11] The structure of such fingers is strongly analogous to diffusion limited aggregation (DLA),[12] both of which obey Laplacian growth. The second is the capillary fingering,[13,14] which appears during slow displacement when the dynamics is controlled by the disorder in the capillary forces related to the pore size distribution. The structure of capillary fingers is different than that of the viscous fingers and can be modeled by the invasion percolation theory.[15,16] An early but detailed study on the crossover between different regimes due to the competition of the viscous and capillary effects can be found in Lenormand *et al.*[17,18]

If both the immiscible fluids are injected simultaneously, and the flow is allowed to settle into a steady state, meaning that the macroscopic flow variables fluctuate around well-defined and constant averages, we have yet another type of flow that differs from the unstable patterns described above.[19,20] Albeit less studied than the non-steady flows, it is a key ingredient in upscaling, see, e.g., Ref. 3.

Both viscous fingering and capillary fingering share the common feature that the invading fluid remains connected. However, in many two-phase flow scenarios, it is not uncommon that the invading fluid breaks and becomes disconnected. The breakage of the phase in porous media has also been widely investigated.[21] To summarize, three mechanisms are usually invoked. First, there is the Roof snap-off.[22,23]

When the tip of the invading fluid exits a constriction, the curvature at the tip decreases, while the curvature inside the constriction remains high. This induces a pressure difference that might create a back-flow of the defending fluid, which breaks the invading one. Another important mechanism is the pinch-off, where a continuous fluid filament breaks up into smaller parts due to the Rayleigh–Plateau instability.[24] The last mechanism, the so-called dynamic breakup,[25] occurs when the tip of a phase encounters a junction of two pores, where it might split to invade both and disconnect then the other phase. Despite the abundant literature on the subject, it remains difficult to establish the effective role and relevance of these mechanisms in both generating and propagating foams in porous media. For example, in the last years, pore network simulations have shown[26] that strong foam generation can occur without the necessity of Roof snap-off mechanism.

Phase breakup is of particular interest to generate foam inside the porous structures.[27] A particular application of foam flow is, for instance, the enhanced oil recovery. As discussed above, displacing a more viscous fluid (e.g., oil) by a less viscous one (e.g., water) creates unstable fingerlike preferential paths. In this way, a certain amount of fluid is left in place, altering significantly the recovery. One method to circumvent this problem is to inject foam, which increases significantly the viscosity of the displacing fluid.[28] A consolidated technique consists in injecting gas and water with surfactant, to create the foam *in situ*.[29] The main objective here is to generate strong foam with a low mobility (foam with smaller blob sizes with a large number of lamellae), in opposition to the weak one with a high mobility (large blobs with fewer lamellae).[30–32]

It can be thus noted that the two types of displacement mentioned, continuous front and foam flow, have been widely studied separately in the literature. One would expect, however, that there might be a transition between these two regimes. Notably, it was early reported experimentally and numerically that a condition for generating foam *in situ* is to apply a minimum flow or pressure gradient.[29,31,33] On the other hand, it may be argued that, if the flow is subjected to an imposed pressure, the development of capillary or viscous fingering leads to an evolution of the flow rate, and of the homogeneity of the pressure gradient as well. It is not unlikely that a fingering regime evolves toward a foam displacement. In a recent paper, Eriksen *et al.*[34] observed experimentally a transition from compact displacement to viscous fingering. They find that, in a radial geometry with imposed pressure drop, the invasion front is initially stable and the invading pattern presents an intense blob dynamic typical of foam, but, after a certain radius, the front adopts a viscous-fingering-like shape. It is perhaps useful to point out that, when injecting the fluid at a constant flow rate in the radial geometry, the velocity of the front tends to decrease naturally due to the conservation of mass. If a critical velocity is necessary for the generation of foam, it is not excluded that the latter stops after a certain distance.

It is essential to note that the distinction between foam and viscous fingering is crucial in the context of upscaling to the Darcy scale. Indeed, because viscous fingering has a fractal geometry, it is impossible to determine a representative elementary volume to describe the porous media as a continuum.

The objective of this work is to better understand the transition between the two types of displacements, continuous flow and foam flow. We show that, when injecting a low-viscous fluid into a porous medium filled with a high viscous fluid at a constant global pressure

drop in a rectangular system, under certain conditions, the system shows a transition from the viscous fingering regime to a compact foam flow. In this regime, the invasion starts with viscous fingers. However, as the front advances toward the outlet, the fingers tend to break into small droplets, developing foam after a certain distance from the inlet. We implement a dynamical pore-network model that is capable of modeling both the classical displacement fronts and blob generations. To characterize this transition, we implemented a method for distinguishing the region of viscous fingering from the region of foam development and propagation, measuring the distance of the crossover line from the inlet. Moreover, we showed the effect of the foam formation on both global quantities, namely, the total flow rate and local quantities, like the pressure gradient and the local flow rate. Finally, the origin of this transition is discussed.

II. PORE NETWORK MODEL

Simulations were carried out in the framework of dynamic pore network modeling.[35,36] The pore network we consider here has an underlying geometry of a regular square lattice of $N_x \times N_y$ links as shown in Fig. 1(a), which is tilted by an angle of 45° with the direction of the global pressure drop. The network consists of composite links, which means that each link contains a narrow pore throat in between two wider pore bodies. This is modeled by having links with varying radius along its length, similar to an hourglass shape, like the one drawn in Fig. 1(b). The total porous space of the network is, therefore, contained by all the links, and the nodes represent only the positions of the intersections of the links. We consider all links with identical length l, presenting axial symmetry. The disorder is then introduced into the characteristic radius, r, of the links. Two different distributions for $r > 0$ are considered as follows:

- Uniform distribution is given as follows:

$$\Pi(r) = \begin{cases} 1/a & \text{if } r \in [\bar{r} - a/2, \bar{r} + a/2] \\ 0 & \text{otherwise} \end{cases}. \tag{1}$$

- Rayleigh distribution is expressed as follows:

$$\Pi(r) = \frac{\pi}{2} \frac{r}{\bar{r}^2} \exp\left(-\frac{\pi r^2}{4\bar{r}^2}\right), \tag{2}$$

where $\Pi(r)$ is the corresponding probability density function, $\bar{r}$ is the average radius, and a is the interval width for the uniform distribution.

We restrict to the creeping laminar-flow regime where the Poiseuille law is valid. In that case, if the link is filled with one Newtonian fluid of viscosity μ, the flow rate q_{ij} inside a link in between two nodes i and j depends on the pressure drop, $p_i - p_j$, between the two nodes,

$$q_{ij} = \frac{\pi r_{ij}^4}{8\mu l}(p_i - p_j), \tag{3}$$

where we assumed that the radius does not deviate too much from its characteristic value r_{ij} of the link. In the case of two immiscible fluids present in the same link, Eq. (3) needs to be modified.[37] First, the viscosity μ will be the effective viscosity $\mu_{ij} = \mu_n S_{ij} + \mu_w(1 - S_{ij})$. Here, S_{ij} is the local non-wetting saturation, namely, the fraction of the link length occupied by the non-wetting fluid, while μ_n and μ_w are,
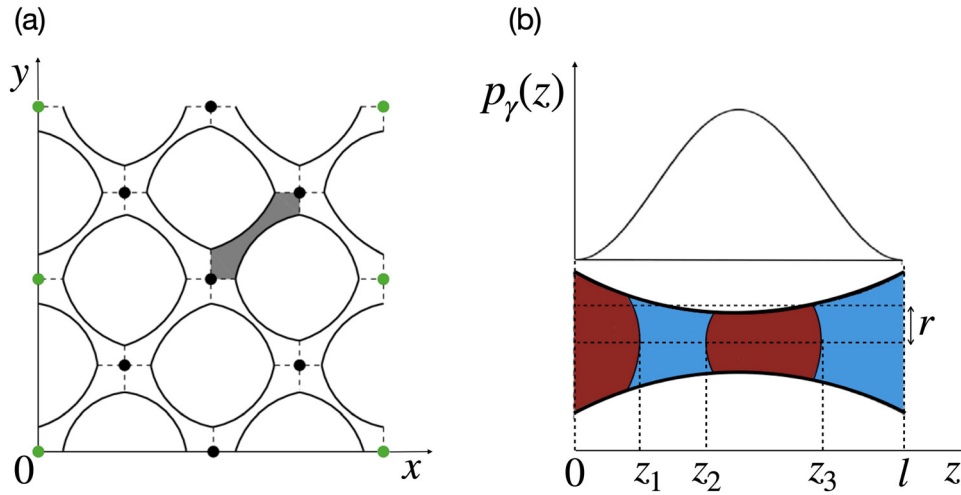
FIG. 1. (a) Illustration of a pore network made by $N_x \times N_y = 4 \times 4$ links. The hour-glass shaped links are connected to each other at nodes denoted by circular dots. Because of the periodicity, green dots at the same height represent the same node. One of the links is colored gray. (b) Illustration of a single composite link filled with two fluids, separated by different interfaces (menisci). The blue color and red color represent the wetting and non-wetting fluid, respectively. The capillary pressure drop for an interface, expressed by Eq. (4), is shown above the link, where $p_\gamma(z)$ is plotted as a function of the interface position $0 < z < l$.

respectively, the non-wetting and wetting viscosities. Second, there is a capillary pressure drop p_γ across the meniscus separating the two fluids that must be taken into account. As the links of the network have a varying radius along their length, p_γ will depend on the position of a meniscus. For the converging–diverging type of an hourglass-shaped link, we model the variation of the capillary pressure with the position $0 < z < l$ of a meniscus by a modified Young–Laplace law,[38,39]

$$|p_\gamma(z)| = \frac{2\gamma}{r_{ij}}\left[1 - \cos\left(\frac{2\pi z}{l}\right)\right],\qquad(4)$$

where $\gamma = \hat{\gamma}\cos\theta$, $\hat{\gamma}$ being the surface tension between the two fluids and θ the contact angle between the meniscus and the link wall, which is assumed not to vary during the motion. With these two modifications, Eq. (3) for a number of m menisci inside a link can be generalized as

$$q_{ij} = \frac{\pi r_{ij}^4}{8\mu_{ij}l}\left[p_i - p_j - \sum_{k=1}^{m} p_\gamma(z_k)\right],\qquad(5)$$

where the summation is over all the interfaces $k = 1, \ldots, m$, inside the link, taking into account the direction of the capillary forces.

We simulate the drainage displacement where a less-viscous, non-wetting fluid invades a network filled with a more-viscous, wetting fluid. This is done by filling the network completely with the wetting fluid initially and then injecting the non-wetting fluid at one edge of the system, marked as inlet ($y = 0$). The opposite edge of the system is marked as outlet ($y = N_y$), through which fluids leave the network. As we perform the simulations at a constant pressure drop ΔP, we impose a fixed pressure value $P_{in} = \Delta P$ at all of the inlet nodes and $P_{out} = 0$ at all of the outlet nodes. This creates an overall global pressure drop ΔP in the direction of the inlet edge to the outlet edge of the network. The two lateral edges of the network parallel to the direction of pressure drop are connected using the periodic boundary condition.

As both the fluids are incompressible, the net volumetric flux of the fluids at any given node will be zero for every time t during the invasion process. This is analogous to the first Kirchhoff law for the electrical current and can be expressed for every node i as

$$\sum_{j\in\mathrm{ngb}(i)} q_{ij}(t) = 0,\qquad(6)$$

where $j \in \mathrm{ngb}(i)$ are the neighboring nodes connected to the node i by links. This provides a closed set of linear equations, which, once solved, allows to compute both the local node pressures $\{p_i(t)\}$ and the flow rates $\{q_{ij}(t)\}$ for the whole network. From the local flow rates, we update the positions of each menisci in the system, displacing it by a distance,

$$\Delta z_{ij} = \frac{\Delta t\, q_{ij}}{\pi r_{ij}^2},\qquad(7)$$

in the direction of the local flow. Here, the time step Δt is chosen in such a way that the largest displacement of any meniscus in any link does not exceed $0.1\, l$ in one time step.

To distribute fluids from links to their neighboring links at the links intersections or nodes, we consider an algorithm that does not impose any restriction on the blob sizes inside any link, and for which the blob sizes are determined by the dynamics of the flow.[40] This makes it possible for the model to generate not only the continuous capillary or viscous fingers but also foams with smaller blobs. The model can, therefore, capture the transition from fingering to foam formations while changing external flow parameters, and no alteration in the fluid distribution algorithms is necessary. We define foam in the context of this model with the presence of the two discontinuous phases in a single link. The algorithm first calculates the total volume of fluids $V_i = -\sum_j q_{ij}\Delta t$ that each node i receives from the incoming neighboring links, namely, the links for which $q_{ij} < 0$ for a node i according to Eq. (5). The individual values of the wetting and non-

wetting volumes V_i^w and V_i^n that the node receives from the incoming links are calculated from the displacements of the menisci following Eq. (7). The two fluid volumes are then redistributed to the outgoing neighboring links, the links for which $q_{ij} > 0$ for any node i. The redistribution follows an impartial rule where the ratio between the total injected volumes of fluids V_{ij} in different outgoing links is equal to the ratio between the flow-rates q_{ij} in those links, and the ratio between the volumes of wetting (V_{ij}^w) and non-wetting (V_{ij}^n) fluids in each individual outgoing link is proportional to the incoming wetting and non-wetting volumes V_i^w and V_i^n in the distributing node. This is done by creating new wetting and non-wetting blobs of volume $V_{ij}^w = q_{ij}\Delta t V_i^w / V_i$ and $V_{ij}^n = q_{ij}\Delta t V_i^n / V_i$, respectively, in every outgoing link of node i. The order of the new wetting and non-wetting droplets is chosen arbitrary. Furthermore, when the number of the blobs exceeds a maximum limit in a link, we merge two nearest blobs keeping the volume conserved, but without detaching any blob attached to a node, which may be a part of a cluster spanned over several links.

In summary, at every time step Δt, we calculate the local pressures p_i for each node and flow rates q_{ij} in each link by solving Eqs. (5) and (6) and then update the positions of the menisci using Eq. (7). The fluids are then exchanged between different links, which in general alters the local saturation S_{ij} in the links, as well as the number and positions of the menisci. This necessitates the linear system of Eqs. (5) and (6) to be solved again in the next time step.

As discussed in the introduction, the main competing mechanisms that control the flow characteristics in two-phase flow are the ratio between the viscosities of the two fluids, called the viscosity ratio, and the ratio between the viscous and the capillary forces at the pore level, known as the capillary number. The viscosity ratio is defined as $M = \mu_n / \mu_w$, whereas the capillary number is generally defined for the flow driven under the constant flow rate Q as[17,38,41]

$$\text{Ca}_Q = \frac{\mu_w Q}{\gamma A}, \tag{8}$$

where $A = N_x \pi \bar{r}^2$ is the average cross-sectional area of the pore network. However, when the system is driven under a constant pressure drop ΔP as we are studying here, the total flow rate Q varies with time. The capillary number is, therefore, defined as a function of the pressure drop,[42]

$$\text{Ca}_P = \frac{\Delta P / N_y}{2\gamma / \bar{r}}, \tag{9}$$

where $\Delta P / N_y$ is the average pressure drop across one link, and $2\gamma/\bar{r}$ is the typical capillary pressure drop for a meniscus in a link. These two dimensionless numbers fully characterize the invasion displacement. This means in particular that different simulations with the same values of M and Ca_P will produce invasion patterns, which are statistically equivalent. In the supplementary material, we show the validity of this statement.

III. TRANSITION FROM VISCOUS FINGERING TO FOAM

Figure 2 displays the evolution in time of a typical invasion front with $M = 10^{-2}$, $\text{Ca}_P = 0.25$, and r uniformly distributed. Unless indicated otherwise, the results presented will correspond to a lattice of size $N_x \times N_y = 200 \times 200$. Here, we describe the evolution of our system using the normalized injected pore volume $\text{IPV} = V_{\text{inj}}/V_{\text{tot}}$, where V_{inj} is the volume of the injected fluid, and V_{tot} is the volume of the total pore space of the network. Initially, the non-wetting phase enters in the porous medium and exhibits the common viscous fingering occurring at a high flow rate.[17] At this early stage, the non-wetting fluid remains continuous in the absence of any breakage. Also, we note that the invaded pores are never occupied again by the wetting phase. However, as the fingers advance through the network, we observe that the continuous non-wetting fingers eventually break up and the invading pattern exhibits a very different foam-like structure composed of many small droplets. The transition happens as a result of the dynamics of the pore network model. There is no separate algorithm for foam formation, and the exact same algorithm that produces fingers also produces foam. Notably, this transition between the continuous viscous fingers to the foam regime appears at a certain distance Λ from the inlet that depends on both the capillary number Ca_P and viscosity ratio M. We will analyze this in detail in Sec. III A.

Figure 3 represents a diagram of the invasion pictures at breakthrough, namely, when the invading fluid reaches the outlet, for different viscosity ratios and capillary numbers for which the foam formation is observed. While for the images at $M < 1$, we observe a proper transition from viscous fingers to foam, in the snapshots obtained setting $M = 1$, the generation of foam occurs immediately after the injection edge, so without passing from the viscous fingering regime. The case of equal viscosities represents then a limiting case.

Restricting to the images at $M < 1$, it can be noted that the distance of occurrence of the transition decreases with both increasing capillary number and increasing viscosity ratio. Both trends can be qualitatively understood. As discussed above, it has been
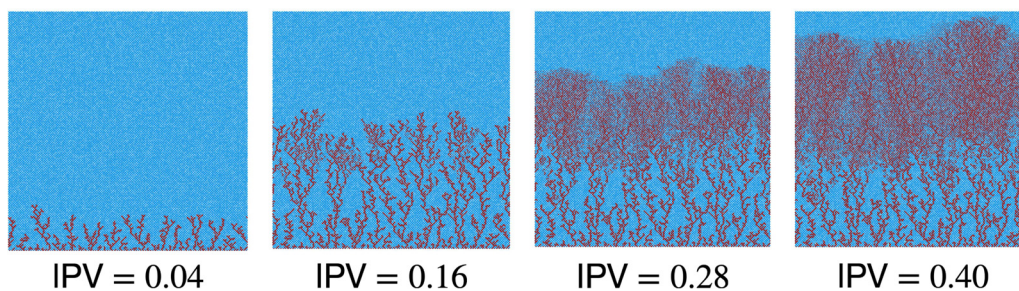

FIG. 2. Snapshots at different growing values of the injected pore volume (IPV). The blue color and red color represent the wetting and non-wetting fluid, respectively. We observe a transition from viscous fingering to foam at a certain distance from the inlet. For this simulation, we set $\text{Ca}_P = 0.25$, $M = 10^{-2}$, and r generated according to the uniform distribution (1) with $\bar{r} = 0.25\,l$ and $a = 0.15\,l$.

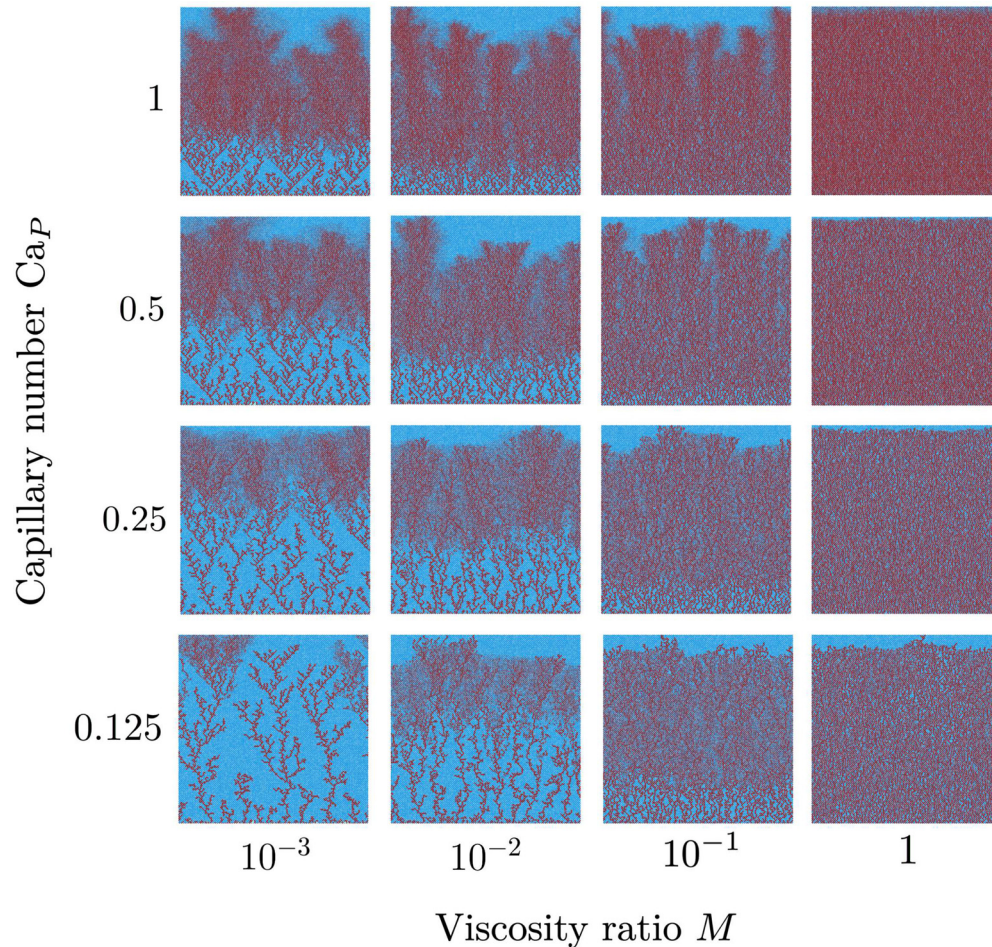| IPV = 0.04 | IPV = 0.16 | IPV = 0.28 | IPV = 0.40 |

FIG. 3. Diagram of the invasion patterns at breakthrough for different viscosity ratio and capillary number. The blue color and red color represent the wetting and non-wetting fluid, respectively. For these simulations, r is generated according to the uniform distribution (1) with $\bar{r} = 0.25\,l$ and $a = 0.15\,l$.

observed[29,31,33,34] that a certain critical pressure drop is required to generate foam. During an invasion process, we can conjecture that the foam is generated in the vicinity of the invasion front, so we should consider the pressure drops across the links close to the front and consider their evolution during the invasion. We remind the reader that we keep the pressure drop between the inlet and the outlet fixed, and since we are injecting a fluid that has much lower viscosity than the defending fluid, the pressure gradient across the non-invaded part of the system increases as the front advances. The local pressure drops across the throats located just after the front will, therefore, increase as well, explaining why foam is triggered only after the front reaches a certain distance from the inlet. Moreover, the pressure gradient rises with both the parameters Ca_P and M. Increasing either the capillary number or the viscosity ratio should then trigger the foam at a shorter distance from the inlet. One might guess that the height of the location of foam generation decreases with the inverse of both the capillary number and the viscosity ratio, namely, $\Lambda \propto Ca_P^{-1}$ and $\Lambda \propto M^{-1}$. However, as we will see in Subsection III A, where we present a method to characterize and analyze the transition distance Λ, this is not the case.

A. Characterization of the fingering-to-foam transition distance Λ

To analyze the transition from viscous fingering to foam, we first need to define a method that differentiates the two regions. For this, we define a quantity $t_{ij} = |S_{ij} - 1/2|$ for every link. This is because, for a continuous displacement pattern, this quantity should be equal to $1/2$, as every link will be fully saturated by either of the two fluids and S_{ij} will be either 0 or 1. Then, t_{ij} will differ from $1/2$ for a link when it is occupied by both the fluids. To define Λ, we then average this quantity in the direction transverse to the overall flow for a certain normalized distance from the inlet y/l and find a quantity $T(y/l)$ given by

$$T(y/l) = \frac{1}{N_x} \sum_{x=1}^{N_x} \left| S_{ij} - \frac{1}{2} \right|. \tag{10}$$

In order to decrease the noise, we average $T(y/l)$ for a given IPV over different realizations of the disorder given by different radii configurations, and we refer to this average as $\langle T(y/l) \rangle_r$. For all the simulations studied, unless specified otherwise, the average is done over 100 realizations of the radii disorder.
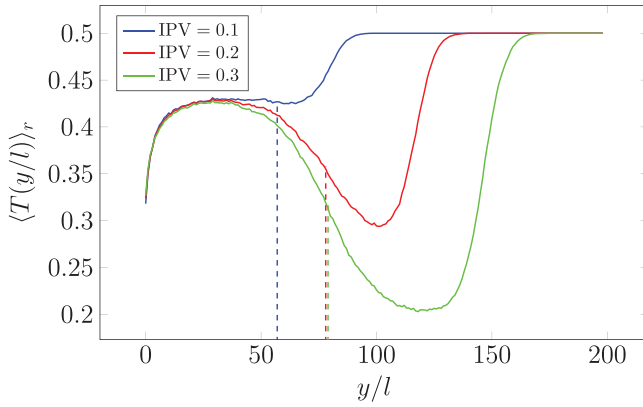
FIG. 4. Plot of $\langle T(y/l)\rangle_r$, defined in Eq. (10), for different growing IPV. For these simulations, we set $Ca_P = 0.25$, $M = 10^{-2}$, and r uniformly distributed according to Eq. (1) with $\bar{r} = 0.25\,l$ and $a = 0.15\,l$. Each vertical dashed line indicates the position of the minimum of the derivative of the curve of the corresponding color, which defines Λ for that IPV.

The typical trend of $\langle T(y/l)\rangle_r$ for different IPV is shown in Fig. 4. For all IPV, and after a short distance from the inlet ($y/l \gtrsim 10$ in the figure), $\langle T(y/l)\rangle_r$ reaches a high value plateau ($\langle T(y/l)\rangle_r \simeq 0.42$ in the figure). This corresponds to the viscous fingering region, where most of the links are saturated by either one of the two fluids. Beyond this plateau, two trends are observed depending on IPV. At lower IPV, before the start of foam formation, there is no decrease in the value of $\langle T(y/l)\rangle_r$, since it increases directly to a higher plateau value of 0.5. This value represents the regions fully saturated by the wetting fluid. At higher IPV, $\langle T(y/l)\rangle_r$ undergoes a significant decrease that characterizes the onset of foam, before reaching again the plateau at 0.5. From this curve, we define the value Λ as the position of the minimum of the curve's derivative, as illustrated in Fig. 4.
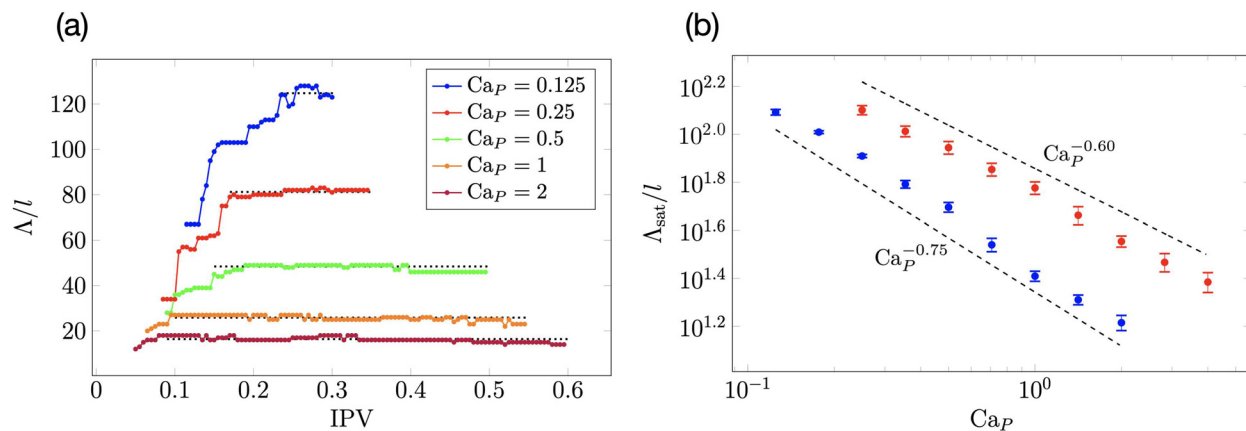
In Fig. 5(a), Λ vs IPV is plotted for different combinations of the capillary number Ca_P. After an initial transient interval, Λ reaches a plateau, where it maintains a constant average value until breakthrough. This value at the plateau depends on Ca_P, and in particular, for higher Ca_P, the Λ plateau is lower and attained sooner. This reflects that the onset of foam formation happens at the earlier stage of invasion with increasing values of Ca_P, as observed in Fig. 3. The plateau value, Λ_{sat}, is then calculated averaging Λ from the end of the transient interval until the breakthrough. In Fig. 5(b), we plot the plateau value Λ_{sat} as a function of Ca_P for the two types of radii distribution, uniform and Rayleigh. We observe a non-trivial power law decay of $\Lambda_{sat} \propto Ca_P^{-\alpha}$. A weighted fit of the data obtained from the uniform radii distribution gives $\alpha \simeq 0.75 \pm 0.03$, while from the data from the Rayleigh radii distribution, we have $\alpha \simeq 0.60 \pm 0.05$. The two trends are represented in Fig. 5(b) with dashed lines. It is worth noting that the simple prediction $\alpha = 1$ discussed in Sec. III is invalidated.

The time evolution of Λ as a function of the viscosity ratio M is shown in Fig. 6(a). Here also, Λ reaches a plateau, where the value at the plateau Λ_{sat} decreases with the increase in M as seen in Fig. 3. We find that Λ_{sat} follows a power-law, $\Lambda_{sat} \propto M^{-\beta}$. For the Rayleigh distribution, a weighted fit for all the data collected returns a power-law $\beta \simeq 0.31 \pm 0.03$. For the uniform distribution, a crossover between two different trends was observed at $M \simeq 10^{-2}$. For the data in the interval $[2.5 \times 10^{-3}, 10^{-2}]$, the fit gives $\beta \simeq 0.25 \pm 0.04$, while in the interval $[\sqrt{2} \times 10^{-2}, 8 \times 10^{-2}]$, we measured $\beta \simeq 0.45 \pm 0.02$. In Fig. 6(b), these trends are highlighted with dashed lines.

The independence of the power law exponents, found for both Ca_P and M, on the radii distribution remains an open question. Recently, it was reported in the literature that steady state rheology of two-phase flow depends in general on the pore size distribution. In particular, some physical quantities can vary when changing the shape of the distribution, but remaining constant if we change only the distribution width while keeping the same shape, and vice versa.[43] Here, it seems that the power law is not independent from the type (so, the shape) of the radii distribution chosen, since the values of the

FIG. 5. (a) Plot of Λ/l as a function of IPV for different Ca_P, setting $M = 10^{-2}$ and uniformly distributed according to Eq. (1) with $\bar{r} = 0.25\,l$ and $a = 0.15\,l$. Λ reaches a plateau value Λ_{sat}/l, indicated by a horizontal dotted line, which is determined by averaging the values after reaching the plateau. (b) Λ_{sat}/l for different values of Ca_P. Blue dots correspond to simulations with $M = 10^{-2}$ and r generated according to the uniform distribution (1) with $\bar{r} = 0.25\,l$ and $a = 0.15\,l$. Red dots correspond to simulations with $M = 10^{-2}$ and r generated according to the Rayleigh distribution (2) with $\bar{r} = 0.1\,l$; their trend $\propto Ca_P^{-0.75}$ is represented by a dashed-dotted line. The error bars represent the standard deviation related to the values of Λ/l averaged to obtain Λ_{sat}/l. The dashed lines show the trends found with a weighted fit of the data.
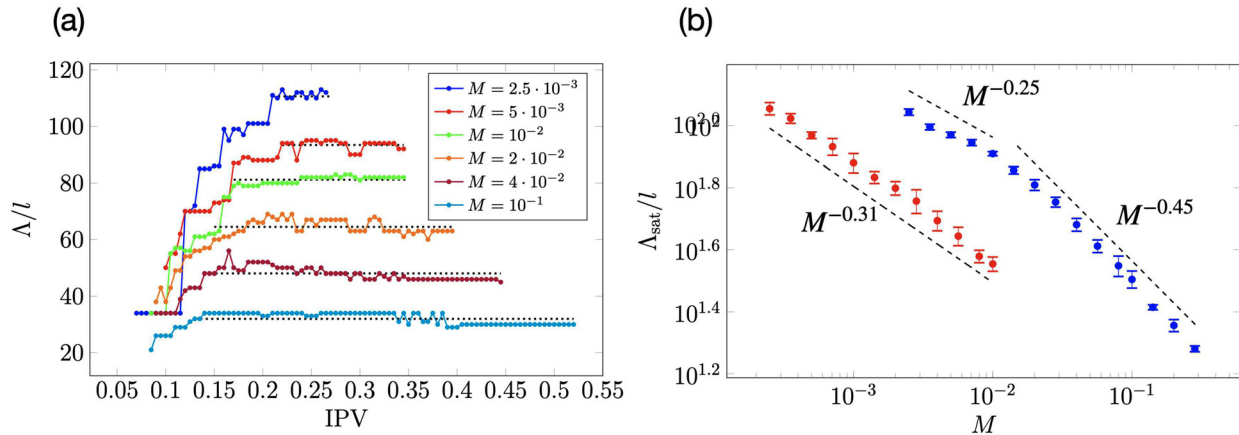
FIG. 6. (a) Plot of Λ/l as a function of IPV for different M, with $Ca_P = 0.25$ and r uniformly distributed according to Eq. (1) with $\bar{r} = 0.25\,l$ and $a = 0.15\,l$. Λ reaches a plateau value Λ_{sat}/l, indicated by a horizontal dotted line, which is determined by averaging the values after reaching the plateau. (b) Λ_{sat}/l for different values of M. Blue dots correspond to simulations with $Ca_P = 0.25$ and r generated according to the uniform distribution (1) with $\bar{r} = 0.25\,l$ and $a = 0.15\,l$. Red dots correspond to simulations with $Ca_P = 0.8$ and r generated according to the Rayleigh distribution (2) with $\bar{r} = 0.1\,l$. The error bars represent the standard deviation related to the values of Λ/l averaged to obtain Λ_{sat}/l. The dashed lines show the trends found with a weighted fit of the data.

exponents measured for the two distributions do not present a good reciprocal compatibility within the error. On the other hand, we have observed that Λ remains constant when keeping the same type of distribution and changing only its width (see the supplementary material).

Now that we have quantified the location of the foam generation, in the following we investigate its influence on the total flow rate.

B. Total flow rate

Figure 7 shows the temporal evolution of the Q-based capillary number Ca_Q, defined in Eq. (8), for different values of Ca_P. Since it is directly proportional to Q, Ca_Q can be thought as a dimensionless total flow rate. Moreover, being the global pressure drop fixed throughout the evolution of the system, the total flow rate for a given IPV can be
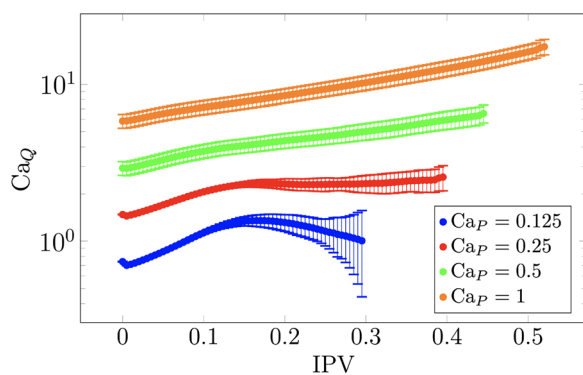

FIG. 7. Plot of the dimensionless total flow rate Ca_Q, defined in Eq. (8), as a function of IPV, averaged over 1000 realizations of the radii disorder, and for different values of Ca_P. The error bars represent the standard deviations of the values collected from the different realizations of the disorder given by the radii configurations. For these simulations, we set $M = 10^{-2}$ and r uniformly distributed according to Eq. (1) with $\bar{r} = 0.25\,l$ and $a = 0.15\,l$.

interpreted as the global permeability of the system. For all Ca_P, initially the flow rate increases due to the viscous fingering instability, as we replace a more viscous fluid with a less viscous one. For later values of IPV, however, we observe an inflection point, which corresponds to the emergence of foam.

We define the inflection point by the change of sign of the second derivative, i.e., a transition between a decreasing slope and an increasing slope (or the opposite). This inflection is more pronounced with lower values of Ca_P. For the lowest capillary numbers studied, the flow rate even seems to be non-monotonic. This is an indication that the generated foam has a very low mobility, which is a typical characteristic of strong foam.[29] Interestingly, we note that, at very low capillary number, the dispersion of the data, represented in Fig. 7 by their standard deviation, becomes very high when the front is close to the outlet.

To better investigate this decrease in mobility, we looked at the evolution of the gradient of pressure along the flow direction. To do this, we average the absolute values of the local pressure drop $dP_{ij} = p_i - p_j$ along the x-direction,

$$|dP_x|(y/l) = \frac{1}{N_x}\sum_{x=1}^{N_x}|dP_{ij}|. \qquad (11)$$

Figure 8(a) shows the time evolution of the normalized quantity $\langle|dP_x|\rangle_r/(2\gamma/\bar{r})$ averaged over different realizations of the radii disorder. Close to the inlet (for $y/l \lesssim 20$), the value is quite high because of our injection condition, where many links contain a meniscus. Further, the gradient of pressure first decreases reaching a minimum and then increases again to reach a plateau value. The lower value region corresponds to the viscous fingering region, where the pressure drop is localized in few channels of low viscosity. The higher plateau closer to the outlet corresponds instead to the region saturated with the defending viscous fluid, hence the higher value. Moreover, as discussed previously, the plateau value increases as the invasion front advances.

Nevertheless, the most important feature is the appearance of a bump after a certain IPV, between the minimum and the plateau,
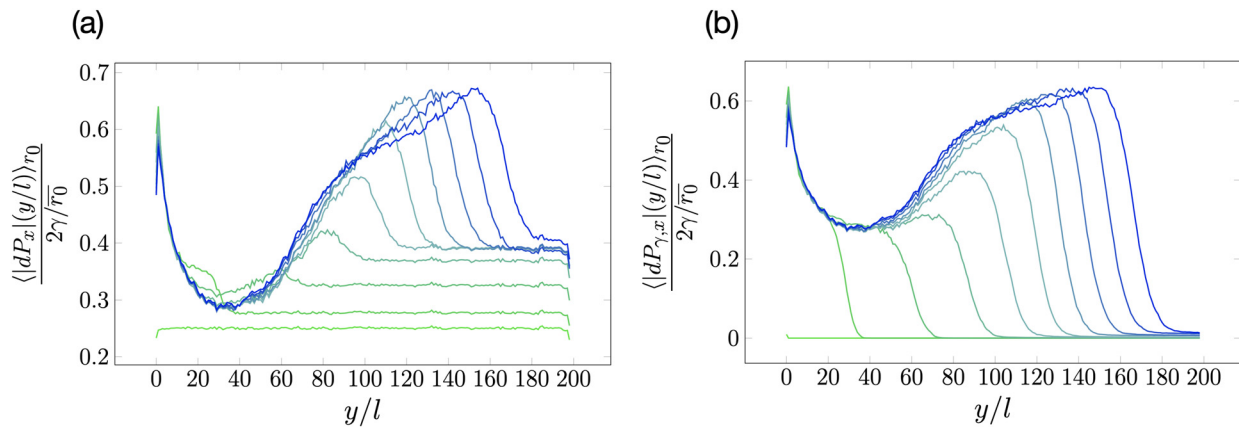
(a)　　　　　　　　　　　　　　　　　　(b)

FIG. 8. (a) Plot of $\langle |dP_x| \rangle_r / (2\gamma/\bar{r})$, as a function of y-position, for different values of IPV. Different color shades represent increasing values of IPV, equally spaced from 0 (light green) to 0.4 (dark blue). The average is done over 100 different realization of the radii disorder. (b) Plot of the capillary contribution $\langle |dP_{\gamma,x}| \rangle_r / (2\gamma/\bar{r})$ of the pressure drop profile pictured on the right at the same IPV. For the simulations for both (a) and (b), we set $Ca_P = 0.25$, $M = 10^{-2}$, and r uniformly distributed according to Eq. (1) with $\bar{r} = 0.25\,l$ and $a = 0.15\,l$.

whose height and width increase as time goes by. This bump corresponds to the foam region, which decreases significantly the mobility of this region. A few observations can be made in this regard. First, the bump starts growing at approximately the same position for different IPV. The location of foam onset is, thus, approximately independent of time, which confirms the stability of the foam generation location. This pressure gradient measurement could thus have been used as an alternative method to quantify Λ. Second, the fact that the bump is higher than the plateau indicates that the mobility of the foam is less than that of the more viscous fluid, despite the foam being highly saturated with less viscous one. This effect is then linked to the presence of menisci in the foam. To quantify the impact of capillarity, we calculate the average of the capillary pressure drops, namely, $dP_{\gamma,ij} = dP_{ij} - 8\mu_{ij}q_{ij}/(\pi r_{ij}^4)$ from Eq. (5), along the x-direction,

$$|dP_{\gamma,x}|(y/l) = \frac{1}{N_x}\sum_{x=1}^{N_x} |dP_{\gamma,ij}|. \qquad (12)$$

In Fig. 8(b), the time evolution of the normalized quantity $\langle |dP_{\gamma,x}| \rangle_r / (2\gamma/\bar{r})$ is shown. Initially, we observe a monotonic decrease between the inlet and outlet, with a sharp drop outlining the displacement front. At a certain time, a capillary pressure bump appears, which is due to foam generation and the occurrence of several menisci. We note that this bump has approximately the same magnitude and evolution as in the previous one, which confirms that mobility loss is mainly due to the presence of many menisci in this region. Another interesting feature is that the curves at different IPV seem to collapse behind the front, just before the onset of the foam, around a local minimum.

C. Foam generation in the pore network

In Subsection III B, we have quantified the occurrence of strong foam and its consequence on the total flow rate. In the introduction, we discussed a crude argument for foam generation, which would occur because the gradient of pressure increases at the tip. However, from this argument, one would expect that the location of Λ decreases like Ca_P^{-1} or M^{-1}, which is not the case. Moreover, by considering the

pressure gradient for different combinations of the parameters, we were not able to identify a clear threshold value of the local pressure drop for the onset of foam. To further analyze the mechanism of foam generation, we show details of few snapshots of very early foam generation in Fig. 9 (upper row). We observe that foam is not necessarily generated at the tip of the front. Instead, blobs are produced by the fragmentation of already developed fingers located also behind the front (like for the one highlighted by the black circle in the last snapshot). In other words, branches created by the viscous fingering might be unstable and fragment at a certain location.

Together with this process of fragmentation, we note that there seems to be an interaction between different growing fingers. As depicted in Fig. 9 (upper row), the fragmentation of a branch is related to the approach of another (the one below on the right side). In Fig. 9 (bottom row), we present the local flow rate field corresponding to the snapshots above by plotting a dimensionless local flow rate defined as

$$\hat{q} = \frac{q\mu_w}{\pi \bar{r}^2 \gamma}, \qquad (13)$$

where q is the local flow rate in a link. The figures show that the fragmentation of the branch occurs together with a decrease in the flow rate in the corresponding links. The flow rate in the approaching finger on the right remains instead approximately constant, so its value becomes higher than that of the breaking finger.

There is, therefore, a competition between the different branches of the invading pattern related to the emergence of foam, meaning that the fragmentation of a branch will stop its expansion, and thus favor the growth of the others. Competition between growing channel in porous media was already observed and studied, also in the context of dissolution in fractured or porous rocks.[44] Furthermore, since the breakage of fingers causes its growth rate to drop significantly, there is a relationship between the creation and propagation of foam and the fluctuations observed in the local flow rate field. In Subsection III D, we measure and characterize the time evolution of the local flow rate both in the finger region and in the foam region.
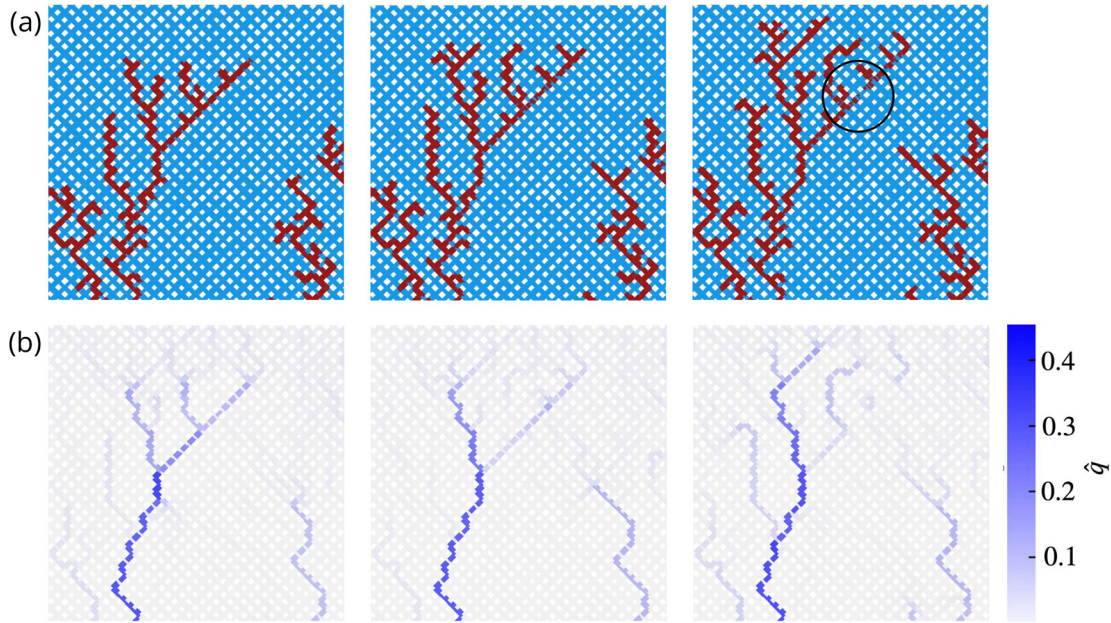
19 February 2024 09:11:08

FIG. 9. Foam creation in the pore network. (a) Detail of different snapshots, at consecutive times from left to right, showing an event of foam formation. The right finger of the bigger branch fragment to create foam, highlighted with a black circle in the rightmost image. (b) Color map of the dimensionless local flow rate $\hat{q}$ defined in Eq. (13) for the respective snapshots above.

D. Fluctuations of local flow rate

Figure 10(a) illustrates the map of the dimensionless local flow rate $\hat{q}$ defined in Eq. (13) for few snapshots close to breakthrough, in a simulation setting $M = 10^{-2}$, $Ca_P = 0.25$, and r uniformly distributed according to Eq. (1) with $\bar{r} = 0.25\,l$ and $a = 0.15\,l$. As expected, in the viscous fingering region, below Λ, the flow is localized in a few, almost parallel channels, corresponding to the branches of the fingers, which were not interrupted during the competition process, mentioned in Sec. III C. The flow rate intensity of a single channel exhibits fluctuation in time, although the average value remains approximately stable and does not drop to zero. On the other hand, above Λ, in the foam region, the main flowing channels fragment into several smaller ones, thus distributing the flow throughout the surrounding links. In this region, new channels are continuously formed and destroyed due to the continuous foam generation led by fragmentation. It results in fluctuations of the local flow rate, which are qualitatively different from the ones in the viscous fingering region. To better investigate these fluctuations in time, we select a single link located in a flowing channel, both in the fingering region and in the foam region. We plot $\hat{q}$ as a function of the normalized time t/T, where T is the total invasion time, for a time interval for which foam is already formed and has reached both links [like in the maps of Fig. 10(a)]. The results are shown in Fig. 10(b) for a link in the viscous finger region, located at $y = y_1 < \Lambda_{sat}$, and in Fig. 10(c) for a link in the foam region, at $y = y_2 > \Lambda_{sat}$. We can see that in both cases $\hat{q}(t/T)$ resembles a stochastic process.

To characterize this stochastic process, Figs. 10(d) and 10(e) show the absolute value of the temporal Fourier transform of the local flow rate, $|\mathscr{F}[\hat{q}](f)|$, for a selected link in the viscous fingering and in the foam region, respectively. We can see that, for the link in the

viscous fingering region, the Fourier spectrum decays approximately as the inverse of the frequency, namely, $|\mathscr{F}[\hat{q}](f)| \propto f^{-1}$, for $f \lesssim 10^{-1}$. This indicates that $\hat{q}$ behaves like a random walk (Brownian) noise, at least for the lower frequencies. On the other hand, for the link in the foam region, the power-law decay occurs approximately as $|\mathscr{F}[\hat{q}](f)| \propto f^{-1/2}$ for $f \lesssim 10^{-1.5}$. An exponent smaller (in modulus) than -1 is typical of anti-correlated signals, and in particular, the exponent $-1/2$ is an indicator of pink noise. As a remark, we report that we performed an analysis, not shown here, of both the local flow rate signals using wavelets and observed results consistent with these obtained by Fourier analysis.

IV. CONCLUSION

In this work, we have investigated the drainage displacement in a heterogeneous porous media. To do this, we used a dynamic pore network model, which takes into account the formation of blobs. We observe that, when the flow is driven by a constant pressure difference between the inlet and the outlet, the displacement front exhibits a transition from a viscous fingering regime to a foam-like region. This transition occurs at a certain distance from the inlet, Λ, which was measured and characterized as a function of the viscosity ratio M and capillary number Ca_P. It has been shown that, after foam is generated, Λ stabilizes to a value, Λ_{sat}, which decreases as a power-law for both parameters. Qualitatively, the occurrence of foam can be explained from the fact that the pressure gradient is not homogeneous through the medium, but is stronger in the defending fluid and is increasing as the front advances. This pressure gradient, in competition with capillary forces, triggers fragmentation and thus foam formation. The onset of foam generation in turn reinforces the pressure gradient increase, leading to the instability manifesting itself as the onset of foam
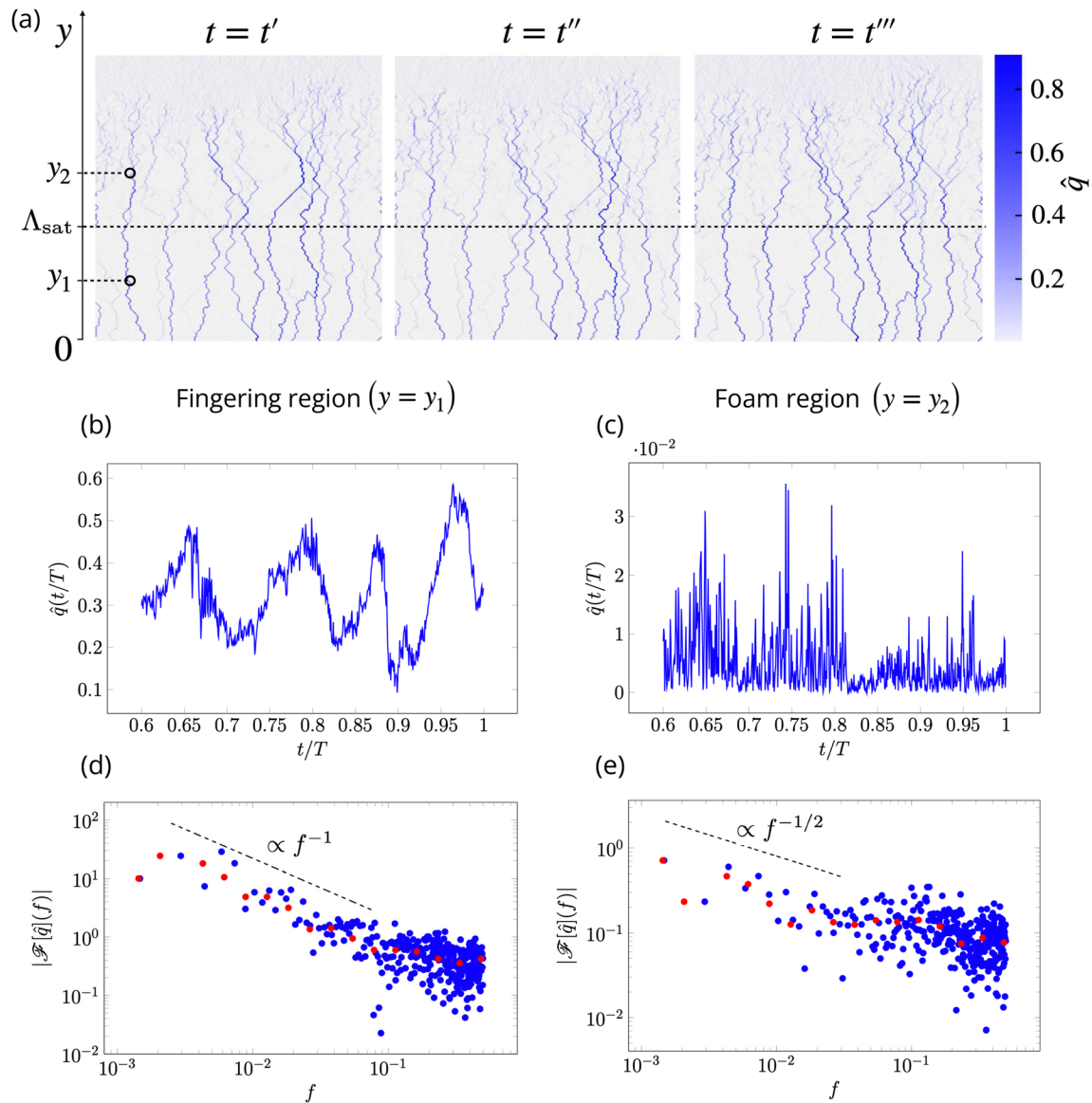
FIG. 10. (a) Color map of the dimensionless local flow rate $\hat{q}$ defined in Eq. (13), at consecutive times $t' < t'' < t'''$. We remind that the main flow occurs in the y-direction. Plot of $\hat{q}$ for a link located at $y_1 = 40\,l$ [(b)] and at $y_2 = 120\,l$ [(c)], as a function of the normalized time t/T in the interval of $0.6 \leq t/T \leq 1$ corresponding to when foam is already present. The positions y_1 and y_2 are highlighted in the first map of (a) by a circle. (d) and (e) Plots of the absolute value of Fourier spectrum $|\mathcal{F}[\hat{q}](f)|$ of the corresponding $\hat{q}(t/T)$ shown above; blue dots represent the values obtained from FFT, while red dots are obtained averaging these values in 20 equally logarithmic-spaced bins in the interval $[10^{-3}, 1]$. All these plots are based on a simulation setting $Ca_P = 0.125$, $M = 10^{-2}$, and r uniformly distributed according to Eq. (1) with $\bar{r} = 0.25\,l$ and $a = 0.15\,l$; the resulting transition distance from the inlet is $\Lambda_{\text{sat}}/l \simeq 79$.

generation. From this qualitative argument, we cannot, however, predict the observed exponents for the power-law decay. Further analysis would be, thus, necessary to understand this transition.

Moreover, we have shown that foam formation could be related to an instability mechanism, with fragmentation of the viscous fingers occurring below the front. We might remark that foam is also responsible for an increase in the local pressure gradient, which in turn should further promote creation of more foam. Furthermore, we

observe that the flow velocity is not homogeneous but localized in few channels, both in the viscous fingers and in the foam region, although in the latter, the channels tend to divide into several smaller ones. This leads to very different behavior of the local flow rate in the fingers region, where the fluctuations are mostly stable in time, from the foam region, where the value drops intermittently to zero. The Fourier analysis suggests that the first resemble a Brownian motion, while the second an anti-correlated (pink) signal. It is clear that the two behaviors

are causally connected, although we still do not understand how the fluctuations in the foam, driven by the fragmentation process, influence the evolution observed in the fingering region, and, eventually, vice versa. However, we can add that the strong fluctuations observed in the foam region can be responsible of the irregular movement of the front observed when foam is formed and is propagating.

We have performed simulations using a constant flow rate Q rather than a constant pressure drop ΔP across the system. In this case, we find no transition zone at any particular location between fingers and foam. Rather, we find that either there are fingers developing all the way through until breakthrough or there is foam generated from the beginning. When imposing constant pressure drop ΔP, the local pressure drop along the system changes as just described. If we define a local capillary number based on this local viscous pressure drop in the constant-ΔP simulations, then we observed that the constant-Q simulations produce only fingers when run with capillary numbers similar to the local capillary numbers in the fingering regimes of constant-ΔP simulations, and they produce only foam when run with capillary numbers similar to the local capillary numbers in the foam regimes of constant-ΔP simulations. The transition from fingering to foam seems, therefore, to be a characteristic of driving the system with constant global pressure drop.

Future research efforts can be dedicated to the experimental observation of the transition and the validation of the predictions elaborated in this work, conceivably building a setup analogous to the one adopted in Ref. 34, in a rectangular geometry. Furthermore, the pore network model presented here can be extended to a three-dimensional domain for comparison with the two-dimensional analysis reported in this study. It is also worth considering the study of two-phase flows where one of the two fluids is non-Newtonian and evaluating the impact of the non-linear rheology, like the presence of yield stress, in foam formation and propagation.

SUPPLEMENTARY MATERIAL

See the supplementary material section, we discuss the independence of the transition height with respect to certain system parameters, showing some snapshots at breakthrough obtained varying these parameters.

AUTHOR DECLARATIONS

Conflict of Interest

The authors have no conflicts to disclose.

Author Contributions

Federico Lanza: Conceptualization (equal); Data curation (equal); Formal analysis (equal); Investigation (equal); Methodology (equal); Software (equal); Validation (equal); Writing – original draft (equal); Writing – review & editing (equal). **Santanu Sinha:** Conceptualization (equal); Formal analysis (equal); Investigation (equal); Methodology (equal); Software (equal); Validation (equal); Writing – review & editing (equal). **Alex Hansen:** Funding acquisition (lead); Investigation (supporting); Supervision (equal); Validation (equal); Writing – review & editing (equal). **Alberto Rosso:** Funding acquisition (lead); Investigation (supporting); Supervision (equal); Validation (equal); Writing – review & editing (equal). **Laurent Talon:** Conceptualization (equal); Data curation (supporting); Formal analysis (equal); Investigation (equal); Methodology (equal); Supervision (lead); Validation (equal); Writing – original draft (equal); Writing – review & editing (equal).

DATA AVAILABILITY

The data that support the findings of this study are available from the corresponding author upon reasonable request.

REFERENCES

[1] J. Bear, *Dynamics of Fluids in Porous Media* (Dover, New York, 1988).

[2] M. J. Blunt, *Multiphase Flow in Permeable Media: A Pore-Scale Perspective* (Cambridge University Press, 2017).

[3] J. Feder, E. G. Flekkùy, and A. Hansen, *Physics of Flow in Porous Media* (Cambridge University Press, 2022).

[4] B. Zhao, C. W. MacMinn, B. K. Primkulov, Y. Chen, A. J. Valocchi, J. Zhao, Q. Kang, K. Bruning, J. E. McClure, C. T. Miller *et al.*, "Comprehensive comparison of pore-scale models for multiphase flow in porous media," Proc. Natl. Acad. Sci. U. S. A. **116**, 13799 (2019).

[5] Y. C. Yortsos, B. Xu, and D. Salin, "Phase diagram of fully developed drainage in porous media," Phys. Rev. Lett. **79**, 4581 (1997).

[6] D. W. v Batenbur, S. Berg, S. Oedai, L. L. David, A. O. Siemens, and K. Elewaut, "Visualisation of light oil mobilisation in ASP core floods using x-Ray CT imaging," *Paper presented at the SPE Asia Pacific Enhanced Oil Recovery Conference* (Kuala Lumpur, Malaysia, 2015).

[7] J. Feder, *Fractals* (Springer, New York, NY, 1988).

[8] K. J. Målùy, J. Feder, and T. Jùssang, "Viscous fingering fractals in porous media," Phys. Rev. Lett. **55**, 2688 (1985).

[9] G. M. Homsy, "Viscous fingering in porous media," Annu. Rev. Fluid Mech. **19**, 271 (1987).

[10] I. C. Salmo, K. S. Sorbie, A. Skauge, and M. A. Alzaabi, "Immiscible viscous fingering: modelling unstable water–oil displacement experiments in porous media," Transp. Porous Med. **145**, 291 (2022).

[11] P. G. Saffman and G. I. Taylor, "The penetration of a fluid into a porous medium or Hele-Shaw cell containing a more viscous liquid," Proc. R. Soc. London, Ser. A **245**, 312 (1958).

[12] T. A. Witten and L. M. Sander, "Diffusion-limited aggregation, a kinetic critical phenomenon," Phys. Rev. Lett. **47**, 1400 (1981).

[13] R. Lenormand and C. Zarcone, "Invasion percolation in an etched network: Measurement of a fractal dimension," Phys. Rev. Lett. **54**, 2226 (1985).

[14] K. Singh, M. Jung, M. Brinkmann, and R. Seemann, "Capillary-dominated fluid displacement in porous media," Annu. Rev. Fluid Mech. **51**, 429 (2019).

[15] D. Wilkinson and J. F. Willemsen, "Invasion percolation: A new form of percolation theory," J. Phys. A **16**, 3365 (1983).

[16] D. Wilkinson, "Percolation effects in immiscible displacement," Phys. Rev. A **34**, 1380 (1986).

[17] R. Lenormand, E. Touboul, and C. Zarcone, "Numerical models and experiments on immiscible displacements in porous media," J. Fluid Mech. **189**, 165 (1988).

[18] R. Lenormand and C. Zarcone, "Capillary fingering: Percolation and fractal dimension," Transp. Porous Med. **4**, 599 (1989).

[19] D. Avraam and A. Payatakes, "Flow regimes and relative permeabilities during steady-state two-phase flow in porous media," J. Fluid Mech. **293**, 207 (1995).

19 February 2024 09:11:08

[20]K. T. Tallakstad, H. A. Knudsen, T. Ramstad, G. Lùvoll, K. J. Målùy, R. Toussaint, and E. G. Flekkùy, "Steady-state two-phase flow in porous media: Statistics and transport properties," Phys. Rev. Lett. **102**, 074502 (2009).

[21]A. C. Payatakes and M. M. Dias, "Immiscible microdisplacement and ganglion dynamics in porous media," Rev. Chem. Eng. **2**, 85 (1984).

[22]J. G. Roof, "Snap-off of oil droplets in water-wet pores," Soc. Petro. Eng. J. **10**, 85 (1970).

[23]W. R. Rossen, "A critical review of Roof snap-off as a mechanism of steady-state foam generation in homogeneous porous media," Colloids Surf., A **225**, 1–24 (2003).

[24]S. Tomotika and G. I. Taylor, "On the instability of a cylindrical thread of a viscous liquid surrounded by another viscous fluid," Proc. R. Soc. London, Ser. A **150**, 322 (1935).

[25]A. C. Payatakes, "Dynamics of oil ganglia during immiscible displacement in water-wet porous media," Annu. Rev. Fluid Mech. **14**, 365 (1982).

[26]M. Chen, Y. C. Yortsos, and W. R. Rossen, "Pore-network study of the mechanisms of foam generation in porous media," Phys. Rev. E **73**, 036304 (2006).

[27]L. Lake, R. T. Johns, W. R. Rossen, and G. A. Pope, *Fundamentals of Enhanced Oil Recovery* (Society of Petroleum Engineers, 2014).

[28]A. H. Falls, J. J. Musters, and J. Ratulowski, "The apparent viscosity of foams in homogeneous bead packs," SPE Res. Eng. **4**, 155 (1989).

[29]T. C. Ransohoff and C. J. Radke, "Mechanisms of foam generation in glass-bead packs," SPE Res. Eng. **3**, 573 (1988).

[30]P. A. Gauglitz, F. Friedmann, S. I. Kam, and W. R. Rossen, "Foam generation in porous media," SPE Improved Oil Recovery Conference, 2002.

[31]D. Tanzil, G. J. Hirasaki, and C. A. Miller, "Conditions for foam generation in homogeneous porous media," in SPE/DOE Improved Oil Recovery Symposium, 2002.

[32]Z. F. Dholkawala, H. K. Sarma, and S. I. Kam, "Application of fractional flow theory to foams in porous media," J. Pet. Sc. Eng. **57**, 152 (2007).

[33]W. R. Rossen, "Theory of mobilization pressure gradient of flowing foams in porous media," J. Colloid Interface Sci. **136**(1), 1–16 (1990).

[34]F. K. Eriksen, M. Moura, M. Jankov, A. L. Turquet, and K. J. Målùy, "Transition from viscous fingers to compact displacement during unstable drainage in porous media," Phys. Rev. Fluids **7**, 013901 (2022).

[35]M. J. Blunt, "Flow in porous media—Pore-network models and multiphase flow," Curr. Opin. Colloid Interface Sci. **6**, 197 (2001).

[36]V. Joekar-Niasar and S. Hassanizadeh, "Critical reviews in environmental science and technology," Critical Rev Environ. Sci. and Tech. **42**, 1895 (2012).

[37]E. W. Washburn, "The dynamics of capillary flow," Phys. Rev. **17**, 273 (1921).

[38]E. Aker, K. J. Målùy, A. Hansen, and G. G. Batrouni, "A two-dimensional network simulator for two-phase flow in porous media," Transp. Porous Media **32**, 163 (1998).

[39]S. Sinha, A. Hansen, D. Bedeaux, and S. Kjelstrup, "Effective rheology of bubbles moving in a capillary tube," Phys. Rev. E **87**, 025001 (2013).

[40]S. Sinha, M. A. Gjennestad, M. Vassvik, and A. Hansen, "Fluid meniscus algorithms for dynamic pore-network modeling of immiscible two-phase flow in porous media," Front. Phys. **8**, 548497 (2021).

[41]O. I. Frette, K. J. Målùy, J. Schmittbuhl, and A. Hansen, "Immiscible displacement of viscosity-matched fluids in two-dimensional porous media," Phys. Rev. E **55**, 2969 (1997).

[42]G. Lùvoll, Y. Méheust, K. J. Målùy, E. Aker, and J. Schmittbuhl, "Competition of gravity, capillary and viscous forces during drainage in a two-dimensional porous medium, a pore scale study," Energy **30**, 861 (2005).

[43]S. Roy, S. Sinha, and A. Hansen, "Role of pore-size distribution on effective rheology of two-phase flow in porous media," Front. Water **3**, 709833 (2021).

[44]M. Hoefner and H. S. Fogler, "Pore evolution and channel formation during flow and reaction in porous media," AIChE J. **34**, 45 (1988).